An Assessment of the Filling Process of the Grand Ethiopian Renaissance Dam and Its Impact on the Downstream Countries

Prakrut Kansara [1], Wenzhao Li [2], Hesham El-Askary [2,3,4,*], Venkataraman Lakshmi [1], Thomas Piechota [2], Daniele Struppa [2] and Mohamed Abdelaty Sayed [5]

1 Engineering Systems and Environment, University of Virginia, Charlottesville, VA 22904, USA; phk5e@virginia.edu (P.K.); vlakshmi@virginia.edu (V.L.)
2 Schmid College of Science and Technology, Chapman University, Orange, CA 92866, USA; li276@mail.chapman.edu (W.L.); piechota@chapman.edu (T.P.); struppa@chapman.edu (D.S.)
3 Center of Excellence in Earth Systems Modeling and Observations, Chapman University, Orange, CA 92866, USA
4 Department of Environmental Sciences, Faculty of Science, Alexandria University, Moharem Bek, Alexandria 21522, Egypt
5 Egyptian Ministry of Water Resources & Irrigation, Cairo 12685, Egypt; abdelaty@mwri.gov.eg
* Correspondence: elaskary@chapman.edu

Abstract: The Grand Ethiopian Renaissance Dam (GERD), formerly known as the Millennium Dam, has been filling at a fast rate. This project has created issues for the Nile Basin countries of Egypt, Sudan, and Ethiopia. The filling of GERD has an impact on the Nile Basin hydrology and specifically the water storages (lakes/reservoirs) and flow downstream. In this study, through the analysis of multi-source satellite imagery, we study the filling of the GERD reservoir. The time-series generated using Sentinel-1 SAR imagery displays the number of classified water pixels in the dam from early June 2017 to September 2020, indicating a contrasting trend in August and September 2020 for the upstream/downstream water bodies: upstream of the dam rises steeply, while downstream decreases. Our time-series analysis also shows the average monthly precipitation (derived using IMERG) in the Blue Nile Basin in Ethiopia has received an abnormally high amount of rainfall as well as a high amount of runoff (analyzed using GLDAS output). Simultaneously, the study also demonstrates the drying trend downstream at Lake Nasser in Southern Egypt before December 2020. From our results, we estimate that the volume of water at GERD has already increased by 3.584 billion cubic meters, which accounts for about 5.3% of its planned capacity (67.37 billion cubic meters) from 9 July–30 November 2020. Finally, we observed an increasing trend in GRACE anomalies for GERD, whereas, for the Lake Nasser, we observed a decreasing trend. In addition, our study discusses potential interactions between GERD and the rainfall and resulting flood in Sudan. Our study suggests that attention should be drawn to the connection between the GERD filling and potential drought in the downstream countries during the upcoming dry spells in the Blue Nile River Basin. This study provides an open-source technique using Google Earth Engine (GEE) to monitor the changes in water level during the filling of the GERD reservoir. GEE proves to be a powerful as well as an efficient way of analyzing computationally intensive SAR images.

Keywords: hydrology; Nile watershed; soil moisture; Sentinel-1; precipitation; Grand Ethiopian Renaissance Dam

1. Introduction

The Grand Ethiopian Renaissance Dam (GERD) is located on the Blue Nile River in Ethiopia, close to the border with Sudan. It was a $4 billion initiative, and with a projected capacity of 6000 megawatts, it is expected to become Africa's biggest power exporter. The Blue Nile impoundment behind GERD will encompass a spatial extent of about 1763.3 km^2 and hold around 67.37 billion cubic meters of water with maximum seasonal load changes

of around 27.93 (41% of total) to around 36.46 billion cubic meters (54% of total) during projected operational scenarios [1]. A study by Elsayed et al. 2020 [2] suggests that the GERD filling and operation would affect the WFE (water, food, and energy) nexus in Egypt, with the impact likely to be significant if the filling process occurred during a dry period. A project of such a magnitude would definitely impact Egypt, whose population is around 100 million and depends on the Nile for about 90% of its fresh water. There is a concern about the risk of drought occurrence that would arise from this project, such as those that affected the Nile Basin in the late 1970s and early 1980s.

A report recently stated that that the GERD reservoir has been expanding—as seen through a series of satellite images [3]. The streamflow in the Blue Nile river has significantly declined since Ethiopia started filling the reservoir [4,5]. This raised some serious concerns in Egypt and Sudan for mainly two reasons—the filling of the GERD reservoir despite no deal being reached during the multi-nation talks and the drought conditions impacting the downstream water bodies [6–8].

There are numerous studies, which suggest that there is a lack of planning for the filling process of the GERD reservoir, especially the consideration of the negative future implications to Egypt and Sudan [9–11]. However, currently, there have been no studies that involve the monitoring of the filling process using satellite remote sensing datasets.

With the increase in technical capabilities and advancements in data processing of satellites, the scientific community has been exploiting the remote sensing capabilities in the estimation of reservoir extent and volume. For instance, a study by Amitrano et al. [12] in 2014 explores the usage of Sentinel imageries in DEM generation, volume estimation and land cover mapping. The study concludes that Sentinel imageries are suitable for volume estimation as well as DEM generation. In addition, Pipitone et al. [13] monitor the water surface level using different remote sensing approaches, including optical imagery (LANDSAT) and SAR imagery. The results from this study show that both optical and SAR imagery techniques can be used to quantify surface water levels.

The motivation for this study is to provide up-to-date and accurate monitoring of GERD filling process using satellite imagery using data from Sentinel-1 and Sentinel-2, and water storage using the Gravity Recovery and Climate Experiment (GRACE), precipitation using the Global Precipitation Measurement Mission (GPM) and topography from the Shuttle Topography Measurement Mission (SRTM). This study will provide a basis for the future management decisions for the operation of GERD that affects the three countries—Egypt, Sudan and Ethiopia. We further investigate the flooding in Sudan on the Blue Nile River Basin and present the impact of GERD on Lake Nasser. We estimate the increase in water storage in the GERD reservoir using SRTM DEM and the Sentinel imagery. To promote the public usability of the research, this study uses an open-source code editor (GEE) to analyze the SAR images as well as uses Python language for analyzing the hydrological datasets. GEE is a cloud-based platform, which is easy to use and can provide quick results without the need to download datasets to a local storage system. With the increasing use of GEE and public availability of datasets and codes, our study will be very useful for future researchers to examine the changes in the volume of the reservoir of GERD.

2. Data and Methods

2.1. Study Area

The GERD is located 15 km East of the Ethiopia–Sudan border inside Ethiopia, on the Blue Nile River (Figure 1). This dam is planned to provide 6.45 Gigawatts of hydro-electric power to Ethiopia at its full capacity and store 67.37 billion cubic meters of water in the Millennium Reservoir formed by the dam. The construction of the dam started in 2011 and was completed in July 2020. The proposed filling of the reservoir has a timeline of 5–15 years depending on the not yet agreed upon trilateral policy agreement between Egypt, Sudan and Ethiopia. The region around the reservoir is a mountainous area with shrubland and forests as the major land cover type. The dam is built on the Blue Nile

River, which is a major tributary of the Nile River. Although the White Nile River is longer than the Blue Nile River, the streamflow in the Blue Nile is significantly higher than in the White Nile. This has created concern for the countries of Sudan and Egypt since they are dependent on the water from the Nile River. Further, the watershed upstream of the dam is referred to as the Upper Blue Nile River Basin.
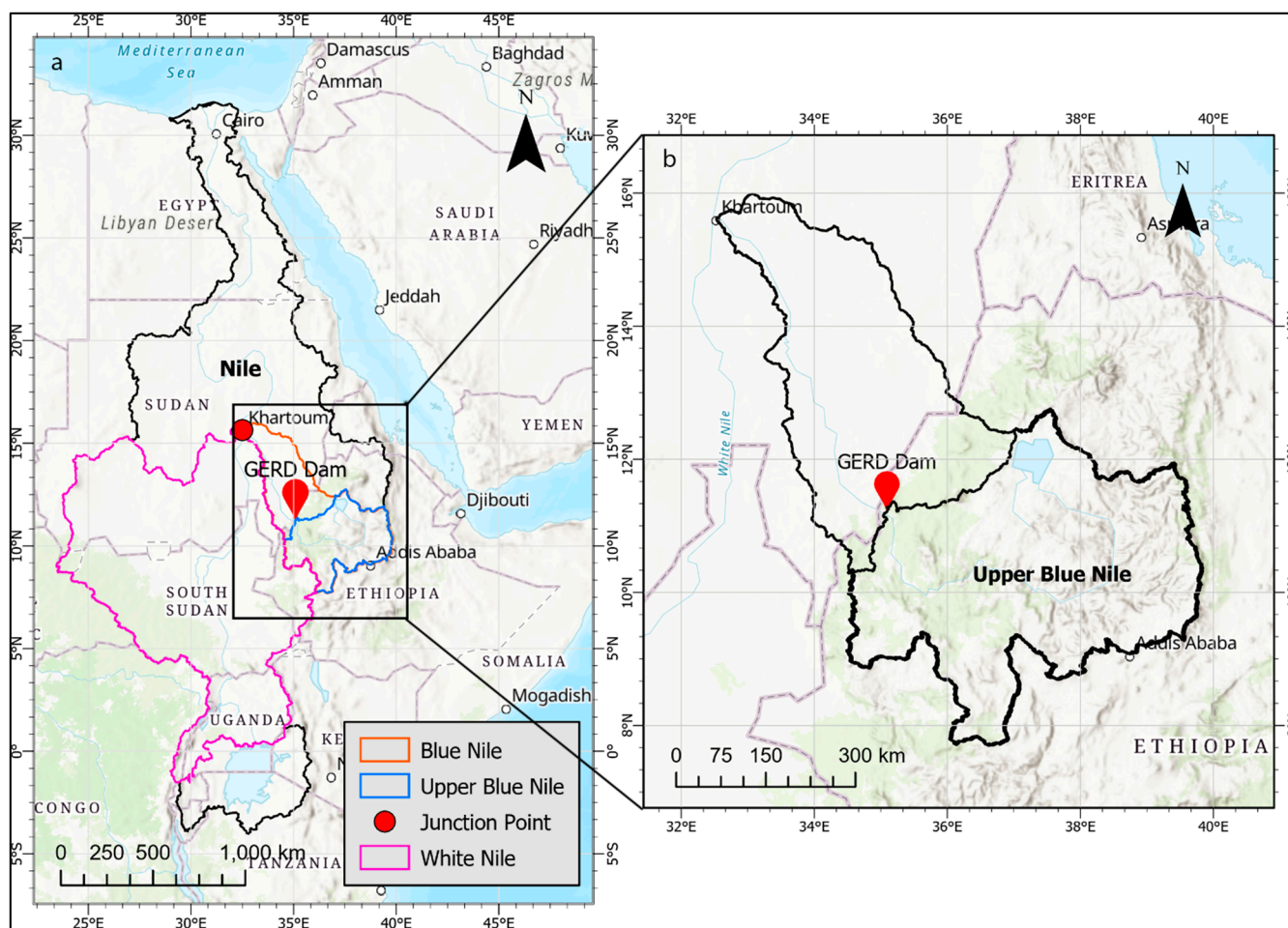

Figure 1. Subfigure (**a**) shows the Nile River Basin and its subbasins—White Nile River Basin and Blue Nile River Basin. The White Nile River and the Blue Nile River merge at Khartoum, Sudan, which is shown as the junction point in the figure. Inset Figure (**b**) shows the Blue Nile River Basin along with the location of the Grand Ethiopian Renaissance Dam (GERD) near the Ethiopian–Sudanese border.

2.2. Data

2.2.1. Satellite Synthetic Aperture Radar and Optical Imagery

In this study, a combination of synthetic aperture radar (Sentinel-1) and optical (Sentinel-2) imagery [12] was used, which could potentially overcome the limitation of exclusive using one type of imagery for the landcover change detection [13]. The Sentinel-1 imagery is obtained from two European Space Agency (ESA) polar-orbiting satellites (Sentinel-1A and Sentinel-1B), operating day and night a C-band (central frequency of 5.404 GHz) synthetic aperture radar (SAR) imaging, with a global revisit time of 6–12 days based on the area. Sentinel-2 is an ESA mission as a constellation with two twin satellites, Sentinel-2A and Sentinel-2B, with a 5 day revisit time. Both satellites carry a multispectral imaging instrument (MSI), which acquires high-resolution optical images in a set of 13 spectral bands of 4 visible, 6 near-infrared and 3 infrared shortwave with 10 m, 20 m, 60 m spatial resolutions, respectively.

2.2.2. SRTM DEM

The SRTM was an international collaboration by NASA in 2000 to map a complete near-global high-resolution data of Earth's elevation [14]. This one-time mission mapped the topography of the Earth's surface using radar interferometry through a two-antenna setup onboard satellite. The elevation difference at nadir location obtained through interferometry is transformed into the digital elevation model (DEM). SRTM void filled 1/3 arc-second data were used for our study.

2.2.3. GPM Precipitation

GPM provides global observations of rainfall and snow using a network of satellites launched by NASA, JAXA, CNES, ISRO, NOAA, and EUMETSAT [15]. This mission was launched in February 2014 with the aim of providing precipitation amount as well as the three-dimensional structure of the storm to better understand the atmospheric structure. The observed data from the constellation of GPM satellites are calibrated with microwave and infrared estimates from other satellite sources to provide high-quality precipitation. This satellite data have improved the forecasting capabilities of disasters like floods and droughts [16,17]. In this study, the Integrated Multi-satellitE Retrievals for GPM (IMERG) Final run version 6 product was used at a spatial resolution of 0.1° for analysis for the period to June 2020 and IMERG Early Run product for analysis from July 2020 to present.

2.2.4. GRACE Total Water Storage

GRACE is a twin satellite setup that measures changes in water anomalies on a global scale [18]. These anomalies depict the changes in the total water column, which includes surface, sub-surface, and groundwater components. This dataset is corrected for atmospheric pressure/mass changes along with the associated glacial isostatic adjustments [19,20]. This dataset has regional errors even after Gaussian filtering [21]. Further details about the data processing and uncertainties pertaining to GRACE data can be found on—https://grace.jpl.nasa.gov/data/get-data/monthlymass-grids-land/. In our study, GRACE RL06 product and GRACE-FO RL06 mascon product from JPL for terrestrial water storage anomalies (TWSA) [22] was used. The data are available at a spatial grid of 0.5° and monthly temporal resolution (https://grace.jpl.nasa.gov/data/grace_months/). In terms of monthly terrestrial water anomalies.

2.2.5. GLDAS Runoff

The global land data assimilation system (GLDAS) is an assimilation model, which combines satellite and ground-based observational data products through different land surface models to generate land surface states and fluxes at a global scale [23]. Five different land surface models are used for the assimilation of parameters and forcing into the models to simulate hydrological variables at the surface and sub-surface level. Full descriptions of each parameter, forcing, and land surface models can be found at https://ldas.gsfc.nasa.gov/gldas/model-output. In this study, total runoff (surface runoff + baseflow) output from the GLDAS V2.1 assimilated data simulated from NOAH LSM model L4 with a spatial resolution of 0.25° at a monthly time step was used. We used the Early Run Product from GLDAS V2.1 outputs for data from July 2020 onwards.

2.3. Methods

2.3.1. SAR Image Processing

In this study, the orthorectified ground range detected (GRD) imagery was collected from both Sentinel-1A/B in IW mode with 10 m spatial resolution. Each image was preprocessed using the following steps: (1) Applying orbit file, (2) GRD border noise removal, (3) Thermal noise removal, (4) Radiometric calibration, and (5) Terrain correction. The band values were converted to the backscattering coefficient ($\sigma°$, dB). The pixels with VV decibel smaller than -18 dB were identified as water pixels. The filling process was presented by false-color images using an enhanced visualization method through

a combination of VV and VH bands. In this study, Sentinel-2 Level-1C data (top of atmosphere (TOA) reflectance) was collected and preprocessed to mask clouds and cirrus areas. The modified normalized difference water index (mDNWI) [24] calculated from the green and shortwave-infrared (SWIR) bands (mNDWI = $\frac{GREEN-SWIR}{GREEN+SWIR}$) with 20 m spatial resolution to effectively differentiate the water and land surface. In addition, the true-color images from China–Brazil Earth Resources Satellite 4 (CBERS) were also used to show the dam filling process.

2.3.2. DEM-Based Estimation of Reservoir Extent

The water volume was calculated for GERD upstream within an area of (35.06°E, 11.23°N, 35.35°E, 10.51°N). The calculation is implemented using Google Earth Engine code editor [25] (see code in supplemental materials). We hypothesized a simple DEM-based estimation of the increase in volume (Equation (1)). Then, per-pixel change in elevation due to an increase in water level (Δh) was calculated. Per-pixel increase in volume is calculated by multiplying the pixel size times the increase in water level (Δh). Δh is determined using the elevation contours from DEM corresponding to the water level as shown in the inset figure (Figure 2). Further, this per pixel calculation was averaged over the entire area where water pixels were detected using the Sentinel images. The mathematical formulation for change in volume is shown below:

$$\Delta V = \Delta h \left(\frac{A_1 + A_2}{2} \right) \tag{1}$$

where ΔV is the increase in the volume of the reservoir storage and A_1, A_2 are the initial and the final surface areas of the reservoir, Δh is the change in the elevation given by the difference in the final and initial height as determined by the DEM. We obtain A1 and A2 from the spatial extent of water pixels estimated from SAR imagery. Moreover, the change in height is obtained from the contour levels obtained from DEM corresponding to the SAR imagery water pixels extent.

2.3.3. Precipitation, Runoff and LWE (GRACE) Analysis

We used IMERG final run data from January 2015 to June 2020, and IMERG Early Run data from July 2020 to December 2020 for precipitation analysis. From the IMERG dataset, the multi-satellite precipitation estimate with gauge calibration was used, which was provided under the "precipitationCal" variable after removing the random errors associated with this precipitation estimate. IMERG provides these errors as a separate variable under "randomError". Further information about the calculation of these errors can be found inside the technical documentation of the dataset (https://gpm.nasa.gov/resources/documents/IMERG-V06-Technical-Documentation). The monthly accumulated values averaged over the watershed area were used to analyze the temporal patterns. The total runoff (surface runoff + baseflow) was calculated using the "Qs_acc" and "Qsb_acc" variables from the model outputs of GLDAS V2.1 with early run products being utilized for data from July 2020 onwards. Since these values were provided as a 3-hour accumulation for a particular month, they were converted to monthly accumulated values. Finally, GRACE liquid water equivalent (LWE) was used for the total water anomaly to observe the changes in the pixel corresponding to the GERD and Lake Nasser locations from April 2002 to November 2020. GRACE and GRACE-FO have missing data from October 2017 to May 2018 due to decommissioning of the GRACE mission. Lastly, the additive model of time-series decomposition was used to remove seasonality from LWE estimates and analyze the trend in seasonality removed observed data.
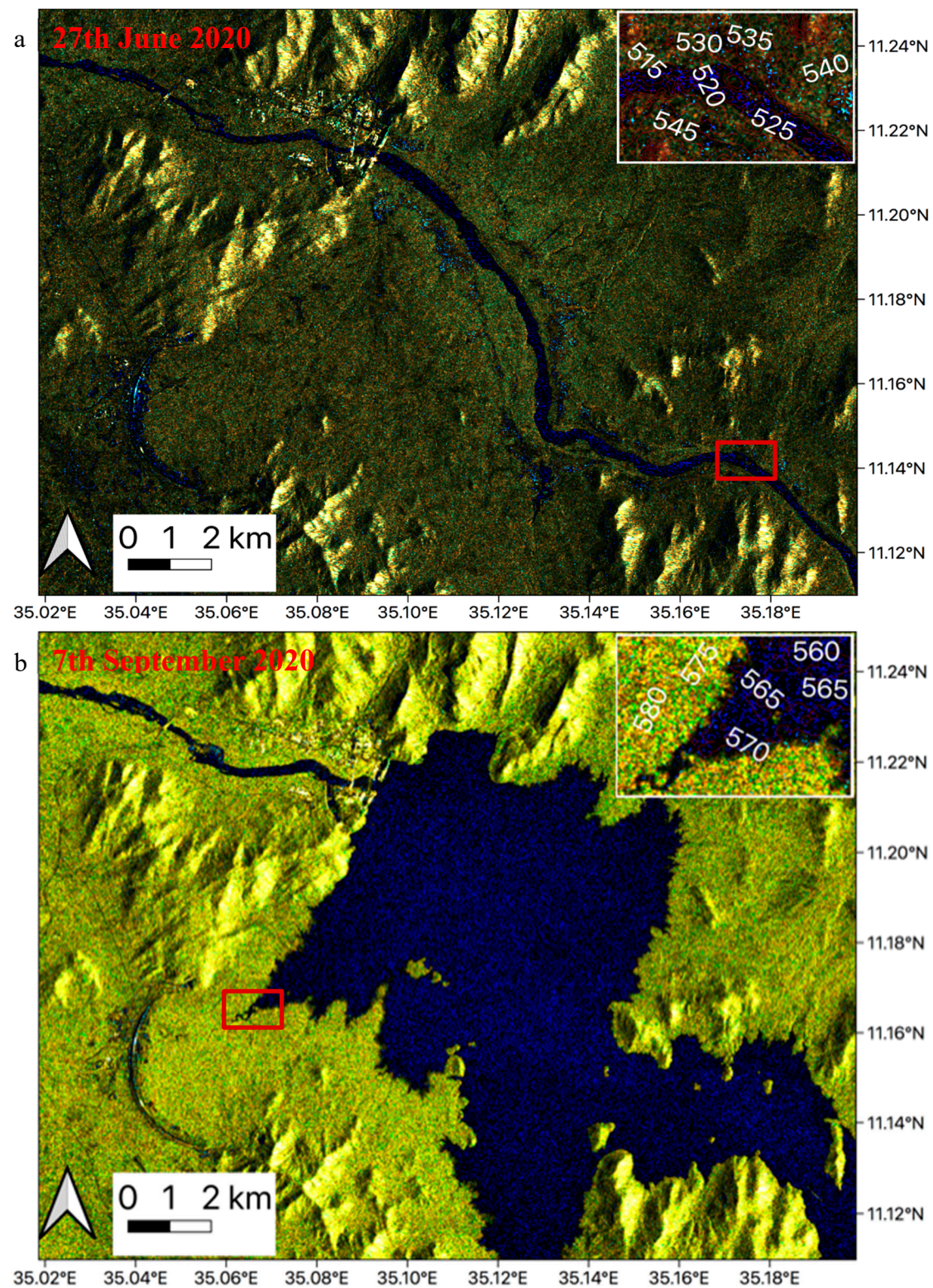
Figure 2. (**a**) Sentinel-1 for 27 June 2020 (prior to the filling process) and (**b**) 7 September 2020 (after the start of the filling process). The increased spatial extent of the reservoir can be observed in the second image on 7 September 2020. The inset figure shows the zoomed view of the region inside the red box to study the elevation contours inside the region. The contour values shown in the inset figure are in meters.

3. Results

3.1. The Monitoring of the Dam Filling

We analyzed the Sentinel-1 SAR images to estimate the filling process of the GERD reservoir. We plotted a series of SAR images to observe the spatial changes in the area covered by water before and after the filling process for the dam (Figure 2). From the SAR image corresponding to 27 June 2020, normal water flow was observed through the river channel for the Blue Nile River. On the other hand, in the 7 September 2020 SAR image significant increase was found in the spatial extent of water-covered areas upstream of GERD. The inset figures in Figure 2 show the elevation contours for the region shown in the red box for each plot to give a sense of elevation around the region. The elevation contours near the river on the 27 June range from 515–545 m, whereas for 7 September, the elevation contour range increased to 560–580 m (an increase of 35–45 m). An increase in the elevation obtained from the DEM corresponds to the rising water level in GERD. To quantify the area changes, the SRTM DEM was used to estimate the increase in the reservoir area during the filling process (Figure 3). We used two SAR images corresponding to 25 September 2019 and 7 September 2020, which represent the reservoir area occupied by water due to the filling process. Further, SRTM DEM was used to construct a spatial map of the increased reservoir area, as shown in Figure 3c. It was found that the reservoir area has increased by approximately 237 km^2, which is 14% of the total surface area of the reservoir (1680 km^2 as estimated at full capacity). In order to track the water level changes during the ongoing filling process, we calculated the estimated from the SAR images (Table 1) based on the observations from the satellite images (see Supplemental Materials). The reservoir filling process started around 8 July 2020 with an estimated water level at 545 m followed by a steady increase in the water levels as indicated in Table 1. From our estimation, the water level at 580 m for the final SAR image on 7 September as analyzed in our study. Overall, the water level increased by 45 m from 27 June 2020 to 30 November 2020. Finally, the calculated estimated increase in the volume of the water stored in the reservoir due to an increase in water level and the areal extent of the reservoir (Table 1). A total increase of 3.584 billion cubic meters from 27 June 2020 to 30 November was found. It was also observed that the increase in volume is significantly higher for late-July and the full month of August as an increase of 1.135, and 1.39 billion cubic meters of water volume was found between 20 July and 14 August 2020, and 14 August and 7 September 2020, respectively.

Table 1. Water level estimated from the digital elevation model (DEM) and corresponding volume of the reservoir.

Date (dd/mm/yy)	Estimated Level (m)	Total Increased Storage ($\times 10^9$ m^3)
27/6/20	520	-
8/7/20	545	0.904
9/7/20	550	1.345
11/7/20	555	1.922
14/7/20	560	2.664
20/7/20	565	3.584
2/8/20	570	4.719
14/8/20	575	6.109
7/9/2020	570	4.719
25/10/2020	567	4.009
30/11/2020	565	3.584

Upstream Sep 25, 2019
Water Level:535 m
Area: 40.29 km2

Upstream Sep 7, 2020
Water Level:572 m
Area: 277.67 km2

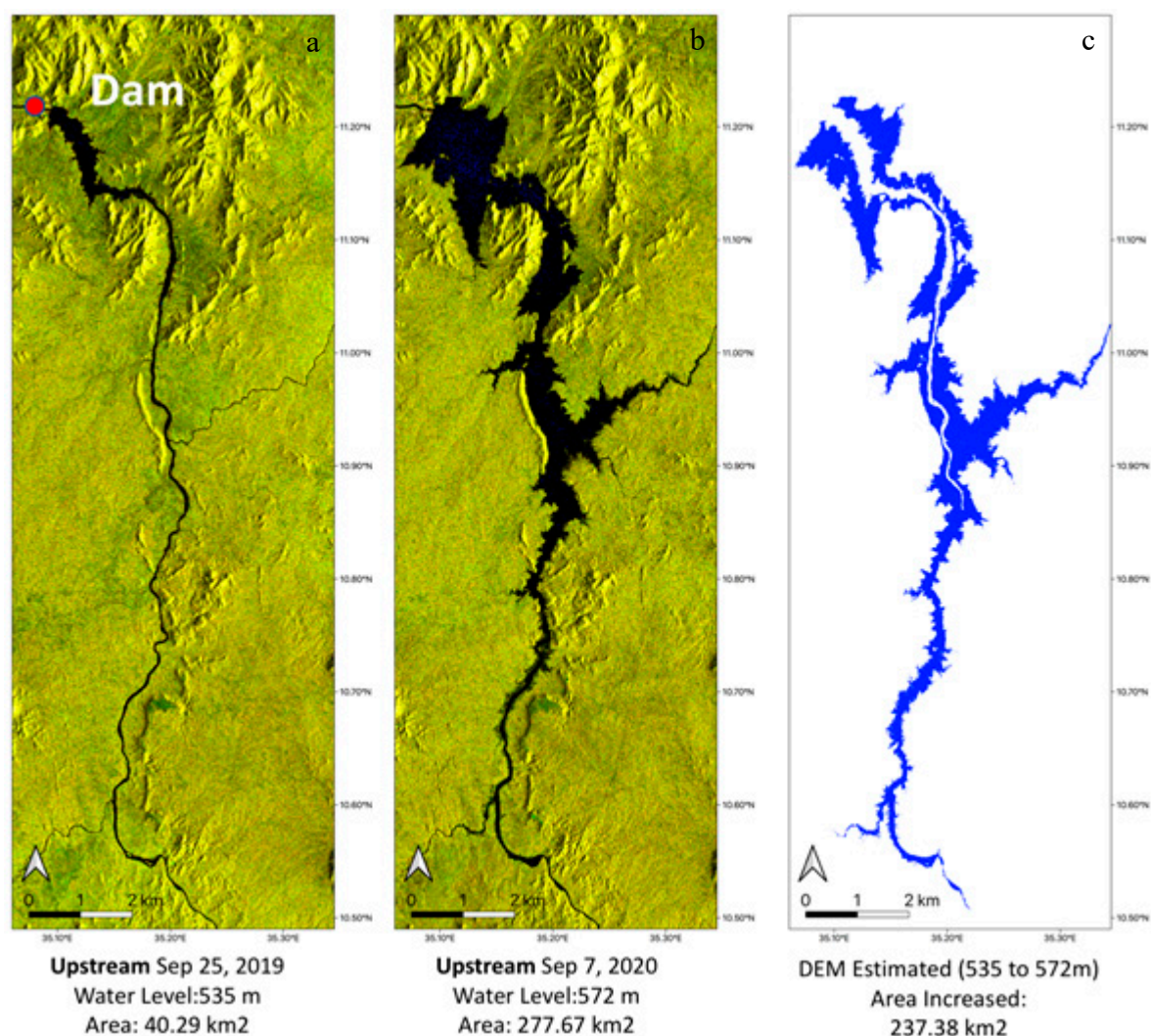DEM Estimated (535 to 572m)
Area Increased:
237.38 km2

Figure 3. (**a–c**) Composite Sentinel-1 images that highlight the spatial extent of the Millennium Reservoir before and after the filling process started. Figure (**c**) depicts the total extent of increased reservoir area as obtained from the digital elevation model (DEM).

3.2. Downstream Impact of Dam Filling

To observe the impact of the filling process of the GERD reservoir on downstream locations, we calculated the number of inundated pixels and plotted the corresponding time-series (June 2017 to December 2020) to compare the increase/decrease of the amount of water on both sides (upstream and downstream) of GERD (Figure 4). Similarly, the water area in one of the areas of Lake Nasser, which is the reservoir of the Aswan Dam in Egypt, was also presented (Figure 5). Additionally, a small region (Figure 5a–c) towards one of the areas of Lake Nasser in Egypt was selected for visual–spatial analysis. To analyze the water inundation near GERD, two regions were selected for the analysis. The upstream region corresponds to a polygon with boundaries at (35.064°E, 11.165°N), (35.087°E, 11.154°N), (35.101°E, 11.220°N), and (35.093°E, 11.221°N) whereas the downstream region corresponds to a rectangular boundary with latitudinal extent of (11.210°N, 11.226°N) and longitudinal extent of (35.054°E, 35.087°E). In Figure 4, it was observed that the upstream of GERD in 2020 had four times the water inundated pixels as compared to the previous three years, with the number of inundated pixels (each pixel area is 900 m^2) increased from approximately four times (2017 to 2020). In addition to this, there was no observed increase/decrease in the inundated pixels at the downstream end of GERD. For Lake Nasser, it was observed that the water inundated pixels showed a stable increase with no notable

changes in the downstream end of GERD. This observation is again corroborated by the Sentinel-2 imagery in Figure 5a–c, where an increase in the water inundation was found at the Southern end of Lake Nasser. The Sentinel-2 imagery corresponds to 18 June 2020, 18 July 2020, and 27 October 2020. This is an interesting observation that the expected increase in water inundation at the downstream end of GERD was not observed. This suggests that there is a need for further investigation of the regional hydrology to understand the anomalous increase in water extent at Lake Nasser. After fitting a second-order polynomial harmonic curve, Lake Nasser showed low water inundation pixels during July 2020 as the GERD reservoir filling process started (Figure 5d). A first-order time-series model was used to fit the trend and seasonality here. The model fitted to the time-series is given below:

$$y = \beta_o + \beta_1 \times t + \beta_2 \times \cos(2 \times \pi \times \beta_4 \times t) + \beta_3 \times \sin(2 \times \pi \times \beta_4 \times t) + e \qquad (2)$$

where β_i are the coefficients estimated by the model, and e is the error term associated with the above estimation model.

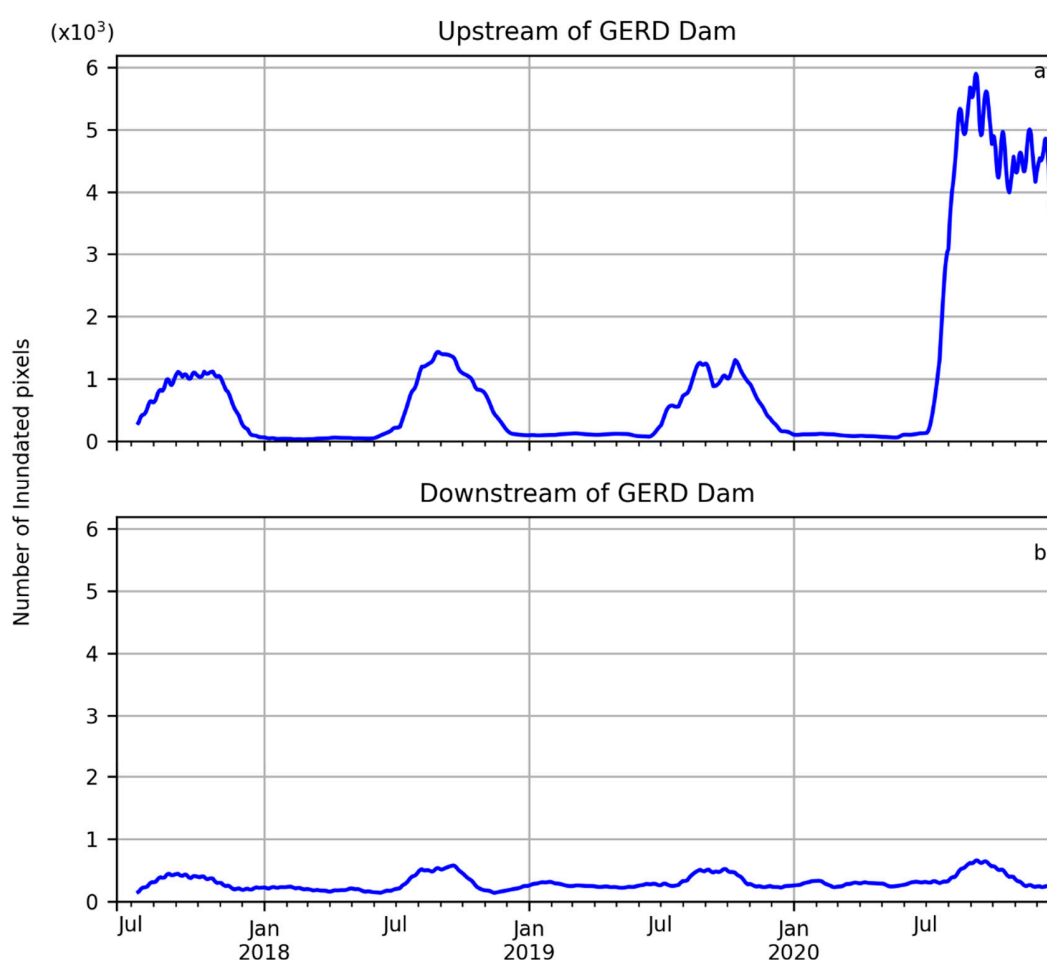**Figure 4.** (**a**,**b**) Number of inundated pixels underwater for selected upstream and downstream locations near GERD as observed from the Sentinel-1 images. The threshold for identifying water/non-water pixels is −18 dB. The upstream region corresponds to a polygon with boundaries at (35.064°E, 11.165°N), (35.087°E, 11.154°N), (35.101°E, 11.220°N), and (35.093°E, 11.221°N) whereas the downstream region corresponds to a rectangular boundary with latitudinal extent of (11.210°N, 11.226°N) and longitudinal extent of (35.054°E, 35.087°E).
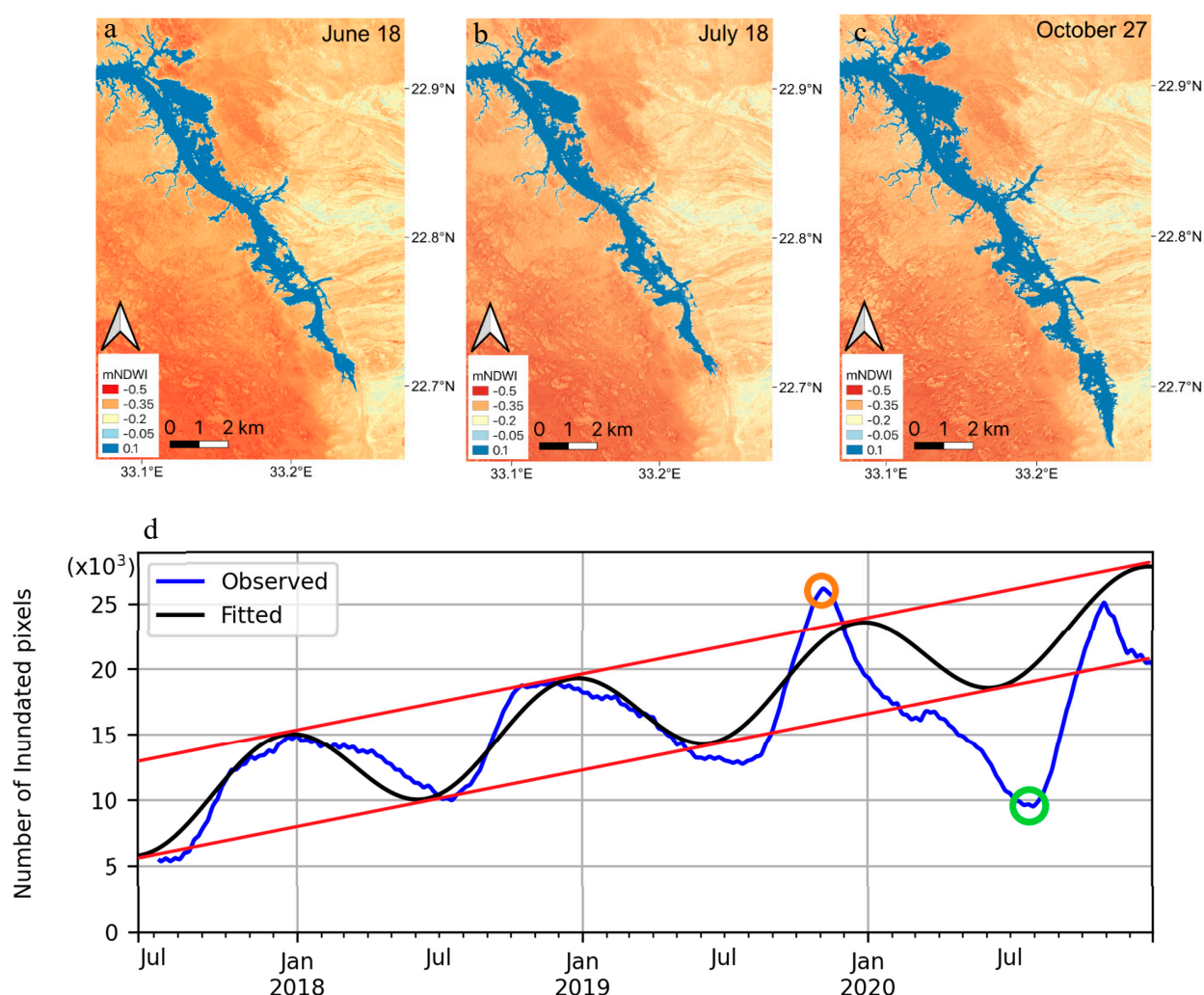
Figure 5. (**a**–**d**) Selected regions of Lake Nasser. Image retrieved from Sentinel-1 and processed to classify water and land pixels using mNDWI. Figure (**d**) shows the water areas represented by pixel counts for the region. Please note that the orange and green circles denote anomalous events. In 2019, Sudan suffered from floods, which impacted the inundated pixels at Lake Nasser. On the other hand, in July 2020, the impact of GERD filling can be seen by the low values of water inundated pixels. The water area in "d" is for a rectangular region with a latitudinal extent of (22.655°N, 22.790°N) and longitudinal extent of (33.169°E, 33.265°E).

In contrast to the fitted curve, which shows a stable increase of water inundation, the observed values show low water inundation pixels during July 2020. Although low water inundation was observed for July 2020, the values for August and September have a lesser deviation from the fitted curve.

3.3. Analysis of Hydrological Variability

To understand the regional hydrology of the Nile river, we analyzed the two most important hydrological variables- precipitation and runoff for the last five years for the Nile River Basin and Blue Nile River Basin upstream of GERD (termed as Upper Blue Nile River Basin) (Figure 6). It was observed that precipitation (370 mm) in the Upper Blue Nile River Basin for the month of August 2020 exceeded the mean precipitation (260 mm) in August for the previous five years (2015–2019) by more than 100 mm. Similarly, the runoff in the Upper Blue Nile River Basin for August 2020 (250 mm) exceeded the mean runoff (110 mm) in the previous five years (2015–2019) by 140 mm. On the other hand, for the Nile River Basin, there was no significant increase/decrease in the precipitation and runoff for 2020 as compared to the previous five years. Furthermore, from the GRACE

total water anomalies for the pixels corresponding to the GERD reservoir and Lake Nasser (Figure 7). Since the signal from desert pixels do not vary over time, the changes captured by the GRACE total water anomaly can be attributed to the changes in water storage for the region. Hence, we use the GRACE data to analyze the trend of overall increase/decrease of water in the region. It was also observed that the deseasonalized data shows an increasing trend for liquid water equivalent (LWE) from 2002–2020. The most recent data available from the GRACE satellite corresponds to November 2020, which is shown as the last value in the figure. For GERD (Figure 7a), it was found that the August anomaly has exceeded the anomalies corresponding to August for the previous five years. This increased anomaly is partly due to the filling up of the reservoir. On the other hand, there was a decreasing trend of GRACE anomaly at Lake Nasser. The absolute magnitude of these anomalies is significantly different, with the magnitude at GERD being higher than Lake Nasser by order of 10.
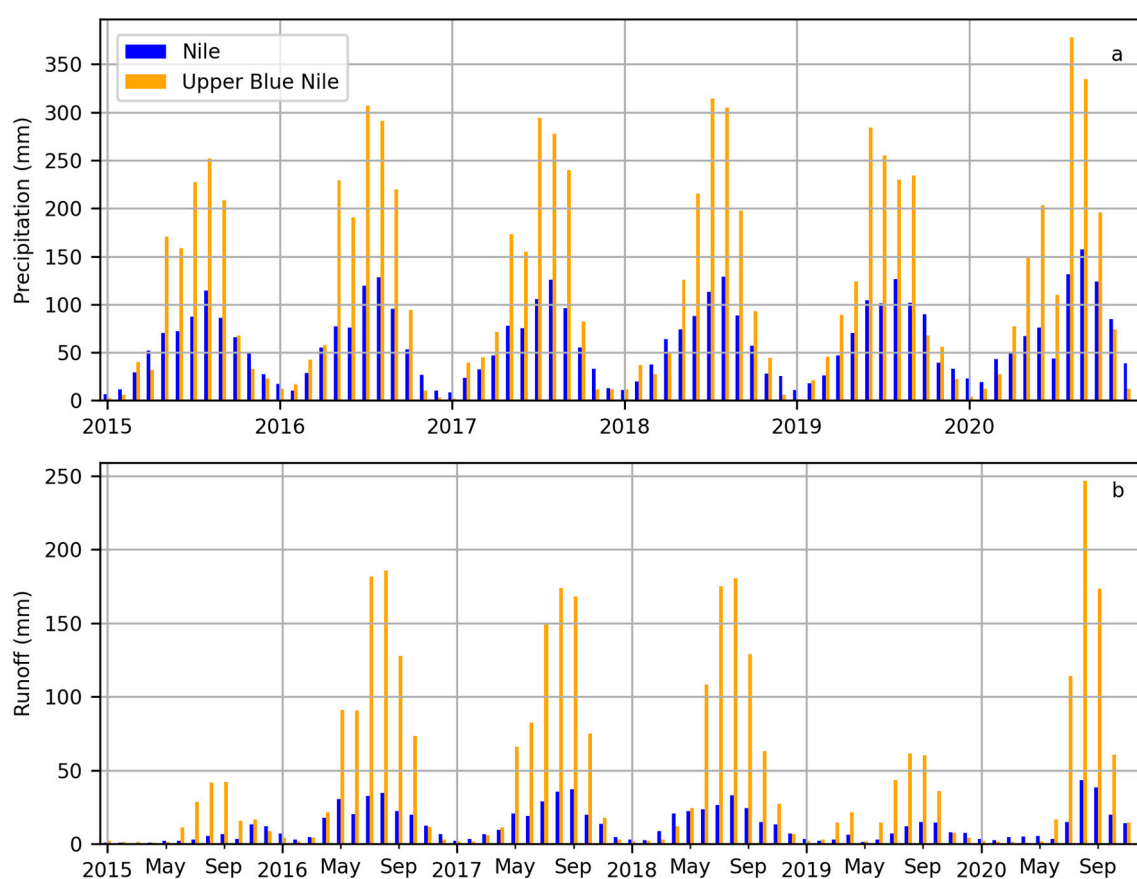

Figure 6. (**a**,**b**) Time-series of precipitation from Global Precipitation Measurement Mission (GPM) data. Figure (**b**) shows the time-series of runoff from the global land data assimilation system (GLDAS). Both figures represent spatially average monthly accumulated values for the corresponding watersheds.
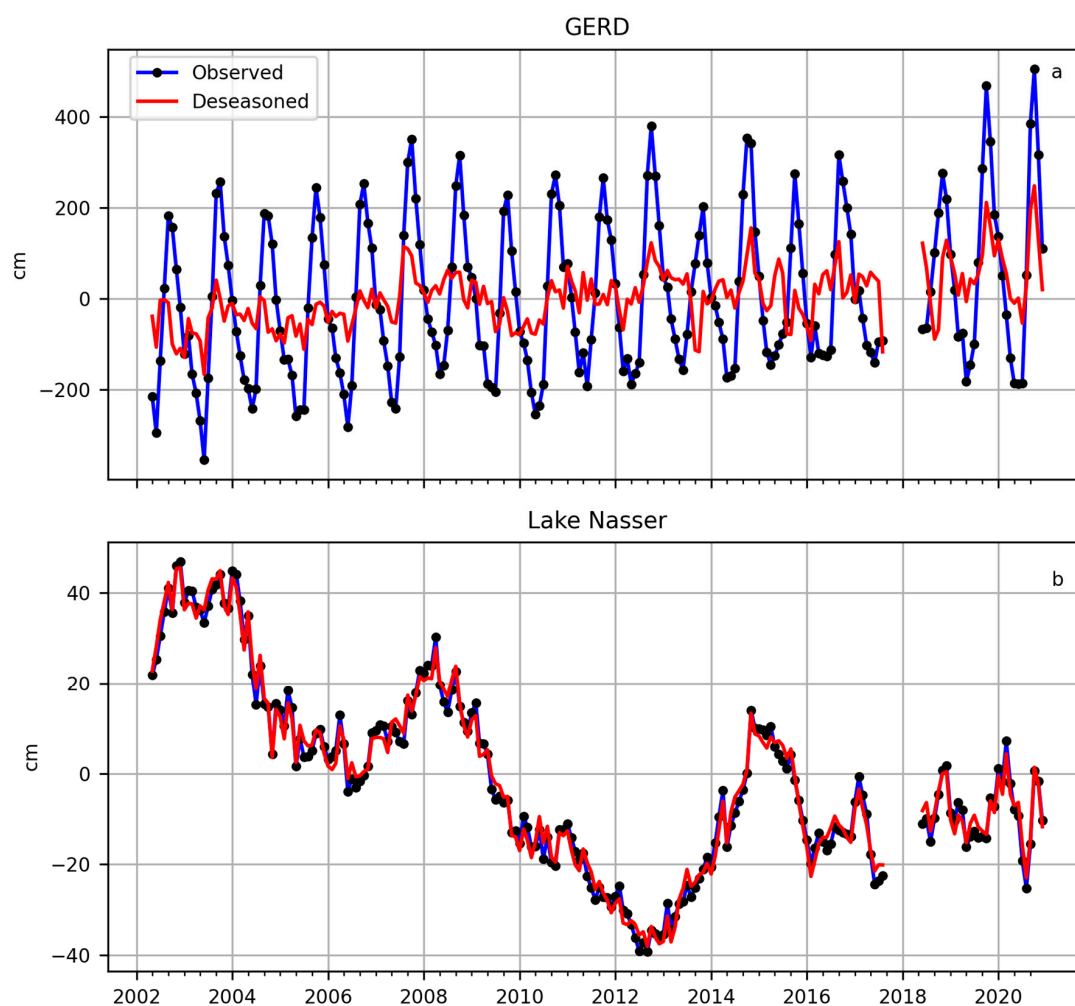
Figure 7. (**a**,**b**) Total water anomaly derived from the Gravity Recovery and Climate Experiment (GRACE) liquid water equivalent (LWE) data for GERD and Lake Nasser. These time-series correspond to the single pixel where GERD and Lake Nasser are located. The GRACE anomalies normalized for the baseline of 2002–2020.

4. Discussion

The construction and filling of GERD have caused disagreements among Ethiopia and the downstream countries of Egypt and Sudan. These countries are situated in the drylands that are vulnerable to water shortage. Our study consists of a simple estimation of the increase in reservoir volume of water (Figure 2 and Table 1) during the filling process. Figure 3 demonstrates the impact of the dam filling on the land morphology and potentially hydrological processes. Meanwhile, we used the most up-to-date publicly available remote sensing data during the time of our analysis. In particular, the synergistic usage of both Sentinel-1 and Sentinel-2 imagery has proved to improve the effectiveness of detecting inundation in this study (Figures 4 and 5). This combination of SAR and optical images can compensate for limitations from each source, such as SAR sometimes misclassifies the areas with low backscattering (e.g., sand) as water, while optical images are strongly affected by atmospheric conditions (e.g., clouds). However, since the SRTM DEM has a spatial resolution of 30 m, any elevation changes inside these 30 m × 30 m pixels will not be accounted for, and thus, the volume estimation is correspondingly under/overestimated. Further, we used satellite datasets, which include data from Sentinel-1 and Sentinel-2, GPM, SRTM, and GRACE, as well as model output from GLDAS. We suggest further studies to consider adding uncertainties to the analysis to understand that may impact the results derived in this study. Further, the runoff data from GLDAS is a model output, which is calibrated globally but lacks calibration at a regional scale. This situation is proved by the

fact that the number of functional hydrometeorological gauging stations declined by 88% between the early 1960s and 2014 [26]. Furthermore, the unusually low number of water inundation pixels (Figure 5d) at Lake Nasser cannot be explicitly explained by GERD filling process since the low values correspond to July 2020 values. Since the dam filling started in early July, it is unlikely that the low inundation is caused by the dam filling process because Lake Nasser is located approximately 1300 km downstream of GERD. Any flow changes in GERD can be observed at Lake Nasser only after a lag of a certain time (in the order of months—flow time between GERD and Lake Nasser), but this study does not contain any such analysis, and we suggest further investigation. In addition, the Early Run IMERG dataset (Figure 6) was used, which is not calibrated with the global rain gauge datasets. Runoff in 2015 and 2019 for the Upper Blue Nile River Basin is lower in 2015 and 2019 as compared to other years despite no decrease in precipitation. This deviation in runoff is caused by the high soil water deficit in Upper Blue Nile and the Nile River Basin. Since there is no runoff due to snow in both of these river basins, soil water deficit becomes a key parameter for estimating runoff [27]. The most recent data for GRACE and GLDAS obtained was for November and December 2020, respectively, at the time of analysis. In Figure 7, the increased GRACE water storage anomaly in August is due to the increased volume of the water in the GERD reservoir. Therefore, we hypothesize that the GERD August anomalies will be sustained for the following months since September precipitation was almost as high as August precipitation, and GRACE anomalies usually lag the precipitation and runoff by around 1–2 months. Studies like the present one where alteration in the natural hydrological processes (such as storage of water in the reservoir) are required to be considered when evaluating water balance and extreme events in large watersheds using satellite observations and model outputs [28].

Recently, Sudan experienced heavy flooding due to a significantly high amount of rainfall during August 2020. This phenomenon was an extreme event, and it coincided with the filling process of the GERD reservoir. Due to the occurrence of such flooding, the actual implications of the shortage of water supply downstream of the GERD reservoir were not observed in our analysis. Due to this excessive flooding, the downstream flow of water into Northern Sudan and Egypt was observed to be significantly higher, which caused the increased water levels in Lake Nasser. Since these extreme events are unlikely to occur every year, consideration of such events should be taken into account using physical-based hydrological models to simulate events where the Blue Nile River receives climatologically average rainfall. The analysis from such a model will be more accurate to provide the basis for policy formulation for the governments of Egypt, Sudan and Ethiopia. Finally, the ground observation networks should be established to support the scientific studies in decision-making and collaborations among the countries in the transboundary basin.

5. Conclusions

This study presents comprehensive monitoring of the filling process of GERD and its implications on the downstream river hydrology. We monitored the spatial extent of the reservoir using Sentinel-1 SAR and Sentinel-2 optical imagery. In addition, SRTM DEM was used to calculate the changes in water depth and increase in the volume of water being stored at the reservoir of GERD. Further, Sentinel-1 imagery was used to calculate the inundated water pixels at the upstream and downstream side of GERD as well as at the southern tail of Lake Nasser. Finally, the precipitation, runoff and GRACE total water anomaly were analyzed for the Nile River Basin and the Upper Nile River Basin. From our analysis, we found that the estimated storage of water in the reservoir has increased by 3.584 billion cubic meters to 30 November 2020, which is approximately 5.3% of the final capacity. In addition to that, we found that the increased reservoir area is already at 14% of the estimated surface area of the reservoir as of 7 September 2020. Further, it was observed that although the number of inundated water pixels did not increase at the downstream end of GERD, there is a significant increase in the water inundation at Lake Nasser. To further investigate the reason behind this observation, precipitation and runoff

in the Blue Nile River Basin were analyzed. We found that the precipitation and runoff for August 2020 were significantly higher for the Upper Blue Nile River Basin as compared to the previous five years. In addition to this, we find an increasing trend in deseasonalized GRACE anomaly for the GERD reservoir, whereas Lake Nasser shows a decreasing trend of anomaly. Finally, the GRACE observations for the month of August and September 2020 show very high anomalies consistent with the very high precipitation and runoff during that month. We conclude that the filling of GERD is not due to natural pooling, and the anomalously high precipitation in the Upper Blue Nile river basin, as well as parts of the Nile River Basin, has attributed to an increase in water inundation at Lake Nasser. Our study shows that the Upper Blue Nile River Basin is experiencing one of the wettest spells, which is overshadowing the negative implications due to dry spells at the downstream parts of the Nile River in Sudan and Egypt. From our observations, we conclude that the current filling process may have drastic downstream implications during dry spells in the Upper Blue Nile River Basin. The dry/wet spells in the Nile River basin have shown direct linkage with the El Niño–Southern Oscillation (ENSO) cycle depicting strong correlations with decadal scale precipitation variations inside the Nile River basin [29]. In addition, this study provides a cloud-based analysis technique to monitor the increase in the volume of water in the reservoir. This method provides easy, computationally light, and quick method for analyzing these datasets. The codes used in this study can be found in the supplementary materials. Finally, we suggest tri-lateral policies for regulating the flow in the Blue Nile River for fair water distribution to the countries of Egypt and Sudan.

References

1.　Madson, A.; Sheng, Y. Reservoir Induced Deformation Analysis for Several Filling and Operational Scenarios at the Grand Ethiopian Renaissance Dam Impoundment. *Remote Sens.* **2020**, *12*, 1886. [CrossRef]
2.　Elsayed, H.; Djordjević, S.; Savić, D.A.; Tsoukalas, I.; Makropoulos, C. The Nile Water-Food-Energy Nexus under Uncertainty: Impacts of the Grand Ethiopian Renaissance Dam. *J. Water Resour. Plan. Manag.* **2020**, *146*, 04020085. [CrossRef]

3.   Siddig, K.; Basheer, M.; Luckmann, J.; Grethe, H. Long-Term Economy-Wide Impacts of the Grand Ethiopian Renaissance Dam on Sudan. In Proceedings of the 22nd Annual Conference on Global Economic Analysis, Warsaw, Poland, 19–21 June 2019.

4.   Salman, S.M.A. The Grand Ethiopian Renaissance Dam: The road to the declaration of principles and the Khartoum document. *Water Int.* **2016**, *41*, 512–527. [CrossRef]

5.   Kahsay, T.N.; Kuik, O.; Brouwer, R.; Van Der Zaag, P. Estimation of the transboundary economic impacts of the Grand Ethiopia Renaissance Dam: A computable general equilibrium analysis. *Water Resour. Econ.* **2015**, *10*, 14–30. [CrossRef]

6.   Zhang, Y.; Erkyihum, S.T.; Block, P. Filling the GERD: Evaluating hydroclimatic variability and impoundment strategies for Blue Nile riparian countries. *Water Int.* **2016**, *41*, 593–610. [CrossRef]

7.   Zhang, Y.; Block, P.; Hammond, M.; King, A. Ethiopia's Grand Renaissance Dam: Implications for Downstream Riparian Countries. *J. Water Resour. Plan. Manag.* **2015**, *141*, 05015002. [CrossRef]

8.   Gebreluel, G. Ethiopia's Grand Renaissance Dam: Ending Africa's Oldest Geopolitical Rivalry? *Wash. Q.* **2014**, *37*, 25–37. [CrossRef]

9.   Basheer, M.; Wheeler, K.G.; Elagib, N.A.; Etichia, M.; Zagona, E.A.; Abdo, G.M.; Harou, J.J. Filling Africa's Largest Hydropower Dam Should Consider Engineering Realities. *One Earth* **2020**, *3*, 277–281. [CrossRef]

10. Dandrawy, M.E.; Omran, E.-S.E. *Environmental Remote Sensing in Egypt*; Springer: Cham, Switzerland, 2020; pp. 533–574. [CrossRef]

11. Wheeler, K.G.; Jeuland, M.; Hall, J.W.; Zagona, E.; Whittington, D. Understanding and managing new risks on the Nile with the Grand Ethiopian Renaissance Dam. *Nat. Commun.* **2020**, *11*, 1–9. [CrossRef] [PubMed]

12. Amitrano, D.; Di Martino, G.; Iodice, A.; Mitidieri, F.; Papa, M.N.; Riccio, D.; Ruello, G. Sentinel-1 for Monitoring Reservoirs: A Performance Analysis. *Remote Sens.* **2014**, *6*, 10676–10693. [CrossRef]

13. Pipitone, C.; Maltese, A.; Dardanelli, G.; Brutto, M.L.; La Loggia, G. Monitoring Water Surface and Level of a Reservoir Using Different Remote Sensing Approaches and Comparison with Dam Displacements Evaluated via GNSS. *Remote Sens.* **2018**, *10*, 71. [CrossRef]

14. Li, W.; El-Askary, H.; Lakshmi, V.; Piechota, T.; Struppa, D. Earth Observation and Cloud Computing in Support of Two Sustainable Development Goals for the River Nile Watershed Countries. *Remote Sens.* **2020**, *12*, 1391. [CrossRef]

15. Farr, T.G.; Rosen, P.A.; Caro, E.; Crippen, R.; Duren, R.; Hensley, S.; Kobrick, M.; Paller, M.; Rodriguez, E.; Roth, L.; et al. The Shuttle Radar Topography Mission. *Rev. Geophys.* **2007**, *45*. [CrossRef]

16. Huffman, G.J.; Bolvin, D.T.; Nelkin, E.J. IMERG Technical Documentation. Available online: https://gpm.nasa.gov/sites/default/files/document_files/IMERG_doc_190909.pdf (accessed on 26 January 2020).

17. Tang, G.; Ma, Y.; Long, D.; Zhong, L.; Hong, Y. Evaluation of GPM Day-1 IMERG and TMPA Version-7 legacy products over Mainland China at multiple spatiotemporal scales. *J. Hydrol.* **2016**, *533*, 152–167. [CrossRef]

18. Tapley, B.D.; Bettadpur, S.; Ries, J.C.; Thompson, P.F.; Watkins, M.M. GRACE Measurements of Mass Variability in the Earth System. *Science* **2004**, *305*, 503–505. [CrossRef] [PubMed]

19. Cheng, M. Correction to "Variations in the Earth's oblateness during the past 28 years". *J. Geophys. Res. Space Phys.* **2005**, *110*. [CrossRef]

20. Swenson, S.; Chambers, D.P.; Wahr, J. Estimating geocenter variations from a combination of GRACE and ocean model output. *J. Geophys. Res. Solid Earth* **2008**, *113*, 08410. [CrossRef]

21. Landerer, F.W.; Swenson, S.C. Accuracy of scaled GRACE terrestrial water storage estimates. *Water Resour. Res.* **2012**, *48*, 48. [CrossRef]

22. Syed, T.H.; Famiglietti, J.S.; Rodell, M.; Chen, J.; Wilson, C.R. Analysis of terrestrial water storage changes from GRACE and GLDAS. *Water Resour. Res.* **2008**, *44*, 44. [CrossRef]

23. Rodell, M.; Houser, P.R.; Jambor, U.; Gottschalck, J.; Mitchell, K.; Meng, C.-J.; Arsenault, K.; Cosgrove, B.; Radakovich, J.; Bosilovich, M.; et al. The Global Land Data Assimilation System. *Bull. Am. Meteorol. Soc.* **2004**, *85*, 381–394. [CrossRef]

24. Xu, H. Modification of normalised difference water index (NDWI) to enhance open water features in remotely sensed imagery. *Int. J. Remote Sens.* **2006**, *27*, 3025–3033. [CrossRef]

25. Li, W. Code for SAR Imagery Processing. Available online: https://code.earthengine.google.com/a794cd8260c2fe1e6f8ce9ff780616c7 (accessed on 25 November 2020).

26. Lv, M.; Lu, H.; Yang, K.; Xu, Z.; Lv, M.; Huang, X. Assessment of Runoff Components Simulated by GLDAS against UNH–GRDC Dataset at Global and Hemispheric Scales. *Water* **2018**, *10*, 969. [CrossRef]

27. Zheng, D.; Van Der Velde, R.; Su, Z.; Wen, J.; Wang, X. Assessment of Noah land surface model with various runoff parameterizations over a Tibetan river. *J. Geophys. Res. Atmos.* **2017**, *122*, 1488–1504. [CrossRef]

28. Lakshmi, V.; Fayne, J.; Bolten, J. A comparative study of available water in the major river basins of the world. *J. Hydrol.* **2018**, *567*, 510–532. [CrossRef] [PubMed]

29. Le, J.A.; El-Askary, H.M.; Allali, M.; Sayed, E.; Sweliem, H.; Piechota, T.C.; Struppa, D.C. Characterizing El Niño-Southern Oscillation Effects on the Blue Nile Yield and the Nile River Basin Precipitation using Empirical Mode Decomposition. *Earth Syst. Environ.* **2020**, *4*, 699–711. [CrossRef]